

# Robotic Tensegrity Structure With a Mechanism Mimicking Human Shoulder Motion

**Lengxue Li**

Electrical and Electronic Engineering,  
Hanyang University,  
Ansan 15588, South Korea  
e-mail: li940513@hanyang.ac.kr

**Sunhong Kim**

Electrical and Electronic Engineering,  
Hanyang University,  
Ansan 15588, South Korea  
e-mail: tjsghd101@hanyang.ac.kr

**Junho Park**

Electrical and Electronic Engineering,  
Hanyang University,  
Ansan 15588, South Korea  
e-mail: somedayif@hanyang.ac.kr

**Youngjin Choi<sup>1</sup>**

Electrical and Electronic Engineering,  
Hanyang University,  
Ansan 15588, South Korea  
e-mail: cyj@hanyang.ac.kr

**Qiang Lu**

School of Automation,  
Hangzhou Dianzi University,  
Hangzhou 310018, China  
e-mail: lvqiang@hdu.edu.cn

**Dongliang Peng**

School of Automation,  
Hangzhou Dianzi University,  
Hangzhou 310018, China  
e-mail: dlpeng@hdu.edu.cn

*This paper proposes a three degrees-of-freedom tensegrity structure with a mechanism inspired by the ligamentous structure of the shoulder. The proposed mechanism simulates the wide motion ranges of the human shoulder joint and is composed of 3 rigid bodies and 16 steel wires with 3 mutually perpendicular rotating axes. Since it belongs to the class 1 tensegrity structure that the rigid bodies do not make any contact with each other, the joint has a certain amount of flexibility, which not only can help protect its mechanism from external impacts but also can prevent human injury that might happen when the mechanism and humans interact each other. Moreover, the proposed mechanism can be manufactured using fewer materials than a fully rigid mechanism, and thus, it can be made in a lightweight fashion and reduce the inertial effects as well. Finally, to actuate the robotic shoulder, the cables connected to each motor are able to drive the rotating shafts of the joint mechanism. [DOI: 10.1115/1.4052124]*

<sup>1</sup>Corresponding author.

Contributed by the Mechanisms and Robotics Committee of ASME for publication in the JOURNAL OF MECHANISMS AND ROBOTICS. Manuscript received April 19, 2021; final manuscript received August 4, 2021; published online September 23, 2021. Assoc. Editor: James Yang.

*Keywords: bio-inspired design, cable-driven mechanisms, compliant mechanisms, control, mechanism design*

## 1 Introduction

Robot has been used in our society as a tool for the augmentation of human activities, and thus human–robot interaction has become a more important issue since the contacts between robots and humans are becoming increasingly frequent in some industrial fields. Although the traditional rigid robot has a high payload and accuracy, it cannot deal with external impacts well, and hidden hazards from surrounding people and the environment exist. To prevent human injury and structural damage when a robot collides with a human, soft robots have begun to attract attention as proposed in Refs. [1–4]. Although many soft robots have the advantage of flexibility, they exhibit problems in terms of accuracy, structural stability due to compliance, and issues such as buckling.

O'Neill et al. proposed a soft wearable robot for the shoulder that combines two types of soft textile pneumatic actuators. Such a robot is lightweight, low-cost, comfortable, and non-restrictive to the wearer, and easy to wear with clothing [5]. Qi et al. proposed a novel soft inflatable arm for a telepresence robot that is capable of imitating the human arm. This robot can handle remote interactions, can interact safely and directly with humans without any external sensors, and is very lightweight [6]. Although such a soft robot is commonly lightweight, flexible, and can guarantee safety in human contact, they have difficulties bearing a large load due to their relatively weak stiffness.

To resolve the problems caused by rigid robots and soft robots, a few researchers have designed flexible joints based on tensegrity. A joint composed of elastic elements and rigid elements might have its own advantages such as the strength of rigid robot and the flexibility of a soft robot. For this purpose, we propose the tensegrity-inspired structure to achieve both softness and rigidity according to the targeted motions. The overall structure of tensegrity consists of tensile elements and compressive elements, using rods (able to bear pressure and compression) and strings (only able to bear tension). Here, rods are similar to human bones, while strings are similar to human ligaments. These joints are operated by electric motors and mechanical cables similar to human muscles and tendons, respectively. Jantsch et al. proposed a robotic arm that is driven by tendons [7]. Similarly, Nakanishi et al. studied musculoskeletal humanoids that are also driven by tendons [8].

Tendon drives have been used not only in robot structures but also in the tensegrity structures. For example, Lessard et al. used shortening and lengthening of the tendon to drive the lightweight multi-axis compliant elbow joint, which is designed based on tensegrity [9]; this research additionally presented two lightweight, elastic, bio-inspired tensegrity arms using a tetrahedron design and saddle design for the shoulder joint. When the joints of these tensegrity robot arms are impacted by an external force, the energy will be transferred into the elastic joints in the arm, which ultimately can reduce the damage to the mechanism. Furthermore, the tensegrity shoulder structure has been proposed in Ref. [10], but it has only two degrees-of-freedom, differently from human shoulder joint. Also, many researchers have used cable-driven joints to construct lightweight mechanism [11] and to ensure the joints have low moving inertia [12], high flexibility [13–16], and adjustable stiffness [17].

In this paper, we propose a three degrees-of-freedom tensegrity structure with a mechanism that can simulate the complex motions of the human shoulder. In detail, Sec. 2 suggests the novel shoulder mechanism. Section 3 shows the mechanism equipped with the electric motor drives. Section 4 explains experimental results. Finally, the paper is concluded in Sec. 5.

## 2 Mechanism Design

Tensegrity structure with a mechanism composed of 16 strings connecting 3 rigid bodies is proposed to simulate the movements

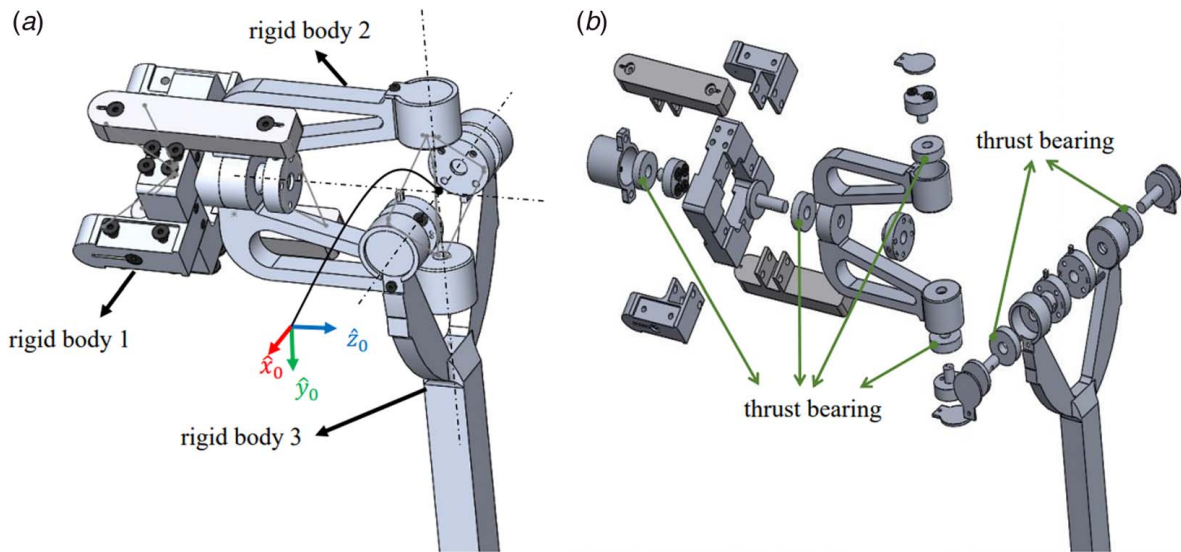


**Fig. 1 The proposed three degrees-of-freedom tensegrity structure with a mechanism: (a) assembled view and (b) unassembled expanded view**

and the ranges of motion of the tensegrity shoulder as shown in Fig. 1. Because all rigid bodies are supported by strings, they do not make contact with each other and belong to the class 1 tensegrity system [18]. This mechanism also has three orthogonal rotation axes as shown in Fig. 1(a).

A set of four strings are used to connect the four vertices at the left end of rigid body 1 and point A of rigid body 2 as shown in Fig. 2(a). To maintain the same tension in the strings, it is necessary to ensure that the four strings are of the same length. And then, second set of four strings are used to connect the two vertices at the right end of rigid body 1 and B, C of rigid body 2, as shown in Fig. 2(b). Since the distance between the fixed points of strings at both ends of rigid body 1 is greater than the distance from point A on rigid body 2 to the line segment  $\overline{BC}$ , rigid body 1 pulls out rigid body 2 to the left and right at the same time. Also, since any pairs of tensions in eight strings have the same magnitudes and opposite directions in the chosen combinations, rigid body 2 is in equilibrium in three-dimensional space. In addition, two mechanical thrust bearings are set in the interior of rigid body 1, so rigid body 2 can rotate about the Z axis.

Third set of four strings are used to connect the two vertices at the right end of rigid body 2 and the two vertices of rigid body 3. The two strings of each vertex at the right end of rigid body 2 are connected to E and D of rigid body 3, respectively. The fourth set of four strings are connected in the same way to opposite side vertices of E and D of rigid body 3. These third and fourth sets of eight strings are of the same length and form an octahedron in three-dimensional space. Each vertex of rigid body 2 and rigid body 3

is provided with thrust bearing; therefore, rigid body 3 can rotate around the X and Y axes.

**2.1 Verification of Human Shoulder Movement and Its Range of Motion.** In the previous section, we proposed the overall structure of the shoulder mechanism. In this section, we show the actual prototype of the proposed design. This study is carried out to verify the proposed design that can simulate human shoulder joints by mimicking the rotation axis and joint constraints. The proposed shoulder mechanism was manufactured using aluminum alloy for the rigid bodies, and then using 7×49 Sava cables (manufactured by Carl Stahl Sava Industries, Inc., minimal breaking tensile strength:  $8.5864 \times 10^8$  N/m<sup>2</sup> and nominal diameter: 0.8128 mm) for the strings to connect these rigid bodies. Six basic movements of the human shoulder are selected from the literature [19], and then these movements as shown in Fig. 3 are simulated by the tensegrity structure with a mechanism proposed in the previous section. In Fig. 3(a), the shoulder is set at the initial posture for motion simulation and medial/lateral rotations are performed utilizing the Y axis of rotation. Abduction/adduction and flexion/extension are conducted as shown in Figs. 3(b) and 3(c), respectively. Indeed, the motion ranges of the human shoulder joint are also suggested in the upper part of Fig. 3, where these joint constraints and ranges serve as a reference for simulation and verification of the proposed biomimetic shoulder mechanism for the six motions in the lower part of Fig. 3.

The results of the manufactured shoulder mechanism inspired by tensegrity showed high similarity to the six motion ranges that a

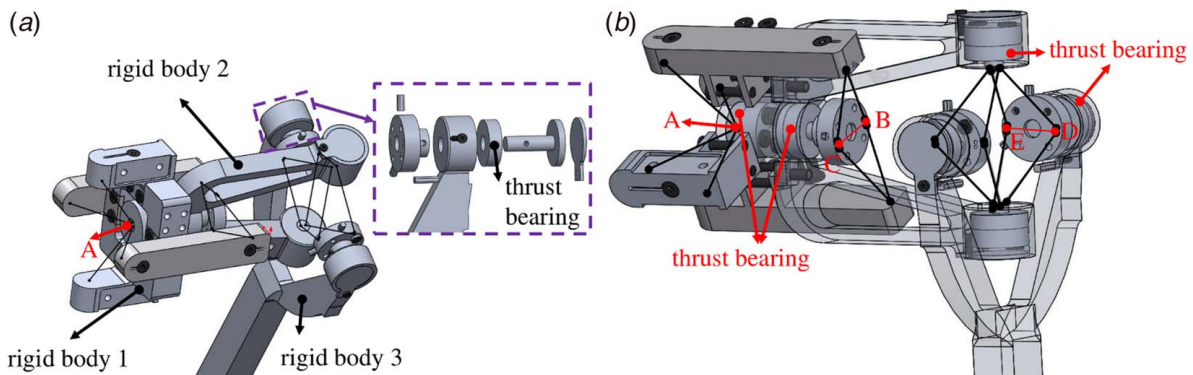


**Fig. 2 Sixteen string configuration of the three degrees-of-freedom tensegrity structure with a mechanism**



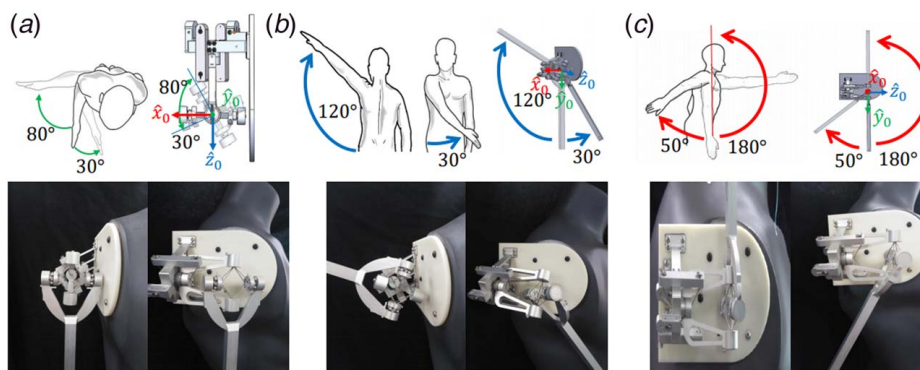


**Fig. 3 Comparison of the ranges of motion between a human shoulder and the proposed tensegrity structure with a mechanism: (a) 0–30 deg medial rotation and 0–80 deg lateral rotation, (b) 0–120 deg abduction and 0–30 deg adduction, and (c) 0–180 deg flexion and 0–50 deg extension**

human shoulder has. These results show how this mechanism can simulate human shoulder motions by studying robotic mechanisms inspired by the human shoulder joints. The next section discusses how to use cables to drive the proposed mechanism.

### 3 Cable-Driven Method With Actuators

In the previous section, we verified that this mechanism can simulate human shoulder movements. The method of using cables to drive this mechanism and the associated cabling configuration are introduced in this section.

**3.1 Cable-Driven Actuation Method.** The cable-driven actuation for the mechanism is designed as shown in Fig. 4. The main method is first explained, and then this same method is repeated to attach the cables to the rigid bodies for actuation. Aforementioned, the proposed tensegrity structure with a mechanism is composed of 16 strings connecting 3 rigid bodies, and the rigid bodies do not contact each other. Because it has three degrees-of-freedom, three electric motors (manufactured by Parker Hannifin) are used to drive the cables so that it can rotate with the Z, Y, and X axes as the rotation axes. In the lateral view, these three motors, labeled as  $M_1$ ,  $M_2$ , and  $M_3$ , are shown in Fig. 4(b);  $M_1$  rotates rigid body 2 around the Z axis via the driving cable,  $M_2$  rotates rigid body 3 about the Y axis, and  $M_3$  rotates rigid body 3 about the X axis. The driving

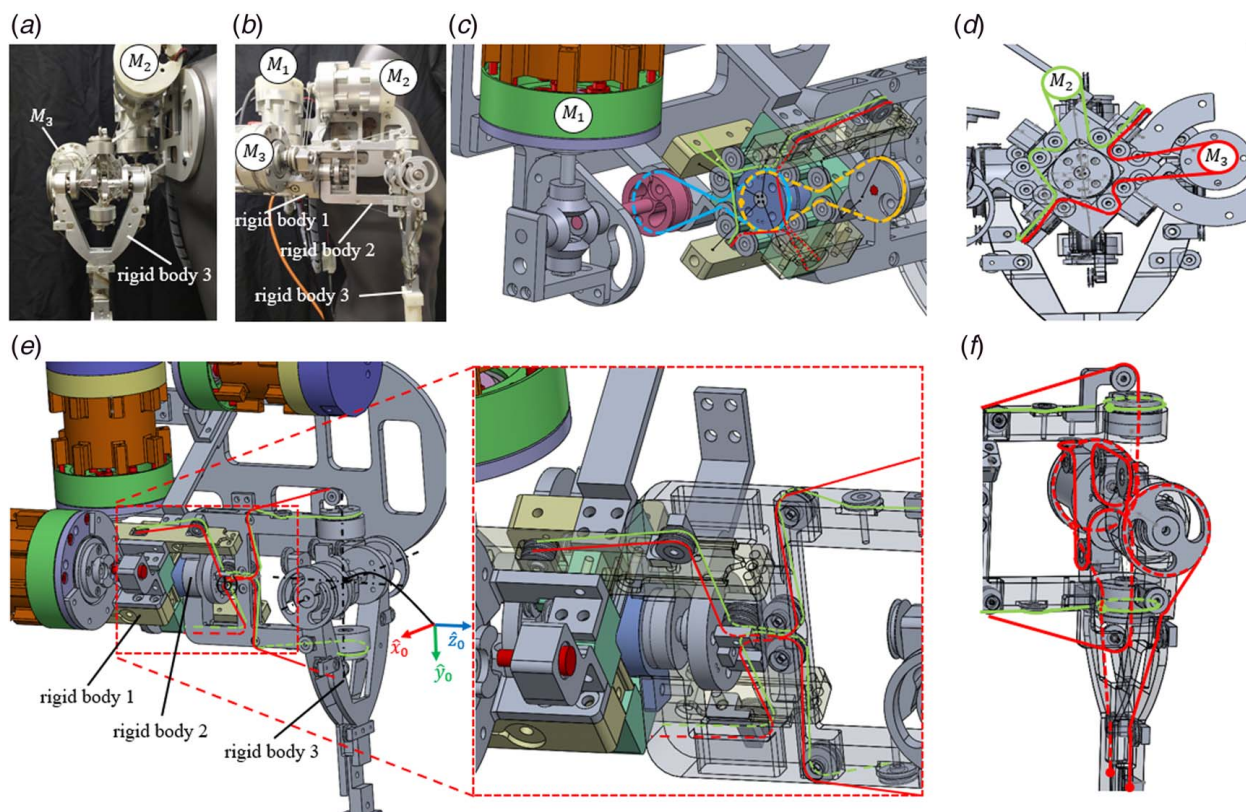


**Fig. 4 Three degrees-of-freedom tensegrity mechanism including cable-driven actuation: (a) frontal view, (b) lateral view, (c) the blue line is connected to  $M_1$ , the green to  $M_2$ , and the red to  $M_3$ , (d) rear view, (e) (left) driving cables denoted by green lines of motor  $M_2$  are connected through the rigid body 1 and those by red lines of motor  $M_3$  through the rigid body 2, (right) zoomed view of the red dotted rectangular area, and (f) cable routes for rigid body 2 and 3 (Color version online.)**

cables that change the direction of power transmission through multiple pulleys are, respectively, connected to three motors as shown in Fig. 4(c); the blue line is connected to  $M_1$ , the green to  $M_2$ , and the red to  $M_3$ .

The rigid body 1 consists of eight pulleys where the upper and lower groups have two pulleys each. Four cables pass through the pulley from the Z-axis rotation center, and two red cables drive the rigid body 3 to rotate around the X axis. Two green cables drive rigid body 3 to rotate about the Y axis. If those cables pass along the center of the rotation axis ideally, the lengths of four cables will not change, even though rigid body 2 rotates around the Z axis. In practice, the four cables cannot pass through the exact Z axis due to their own diameters, but close to the Z axis. Thus, when rigid body 2 turns, the lengths of four cables might change slightly, but it will not affect the rotation of the mechanism because the distance between the four cables and the Z axis is very small and equidistant. On the other hand, the pulleys to change the tensile force directions on the cables are denoted in Fig. 4(e). As the number of pulleys increases, so the difficulty of assembling this structure also increases. Since the increase of the pulley weight is negligible, however, the overall structure is maintained to be relatively lightweight.

**3.2 How to Reduce the Slack.**  $M_1$  drives the cable to rotate around rotation axis 1 (Z axis) as shown in Fig. 5. A pair of bevel gears is used to change the direction of power transfer from  $M_1$ . Then the drive cable is used to connect the output part of the bevel gear and rotation axis 1, so that  $M_1$  can indirectly drive rotating axis 1, as shown in Fig. 5(a). The motor torque will generate a force  $F$  on one side of the cable, so that the force  $F$  generated on the cable pulls and causes rotation around axis 1 along one direction. Since the rotation axis 1 is supported by four tensegrity strings that have a certain amount of elasticity, the strings will be elongated or shortened under force  $F$ , as shown in Fig. 5(b). The right side strings pulling in the opposite direction of  $F$  will become tighter, and the left-side strings pulling in the same direction of  $F$  will become looser, as shown in left one of Fig. 5(b). The red dotted lines of the tensegrity strings indicate the tight state before the motor rotates, and the curved red solid lines at the adjacent positions indicate the slack (or loose) state after the motor rotates.

To resolve the slack issue, new rotation axis was added to the opposite side of  $M_1$  as shown in right side of Fig. 5(b), and the cable is additionally used to connect the rotation axis 1 and

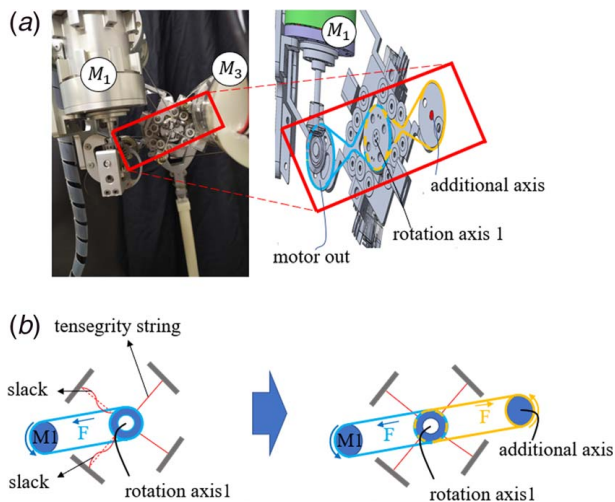


**Fig. 5 Illustration for reducing the slacks of tensegrity strings, where (a) rear view of  $M_1$  driving rigid body 2 to rotate around the Z axis and (b) how to reduce the slacks of strings using an additional rotational axis (Color version online.)**

the additional axis. When  $M_1$  is rotating, a force  $F$  will be generated on the blue cable to make a rotation around axis 1. At the same time, a force equal to the magnitude of  $F$  and opposite to its direction will be generated in the orange cable. In this way, the rotation axis 1 is prevented from the slacks of the strings so that it can reach a balanced state without experiencing severe tension or relaxation at the same time.

**3.3 Payload.** The structure in Fig. 6 is based on the principle that  $M_3$  drives rigid body 3 to rotate about the X axis. The red and pink cables in Fig. 6 are connected to  $M_3$ , and the red cable is pulled with a force  $F$  along the direction shown in Fig. 6, when  $M_3$  rotates. During this process, the red cable is not stressed but the fixed point  $P$  at the end of the red cable is subject to forces  $F$  due to pulling. The force  $F$  at this point is decomposed into a force  $F_1$  perpendicular to the line segment  $\overline{PP_1}$ , and a force  $F_2$  collinear with this line segment. The force  $F_2$  does not make a rotation of rigid body 3, while the force  $F_1$  is always perpendicular to the line segment  $\overline{PP_1}$ . Therefore,  $F_1$  provides a moment for rotation of rigid body 3 around the X axis. At this time, rigid body 3 rotates clockwise around the point  $O_2$  with the moment  $F_1 \cdot \overline{P_1O_2}$ . When the motor  $M_3$  turns in the opposite direction, the red cable has no tension, while the pink cable has tension. At this time, rigid body 3 rotates counterclockwise with respect to the point  $O_2$ . From the perspective of statics, the relationship between the tensile force on the driving cable and the lifted weight (payload) can be analyzed using geometrical decomposition of force vectors.

For this purpose, assume that rigid body 3 is set parallel to the horizontal plane, and one end of the red drive cable is fixed at point  $P$ , as shown in Fig. 7(a). The weight  $W$  due to gravity is oriented vertically downward and then rigid body 3 takes the axis  $O_2$  as the rotation axis. Figure 7(b) shows a schematic diagram of the force analysis of the drive cable. The red line segment shows that

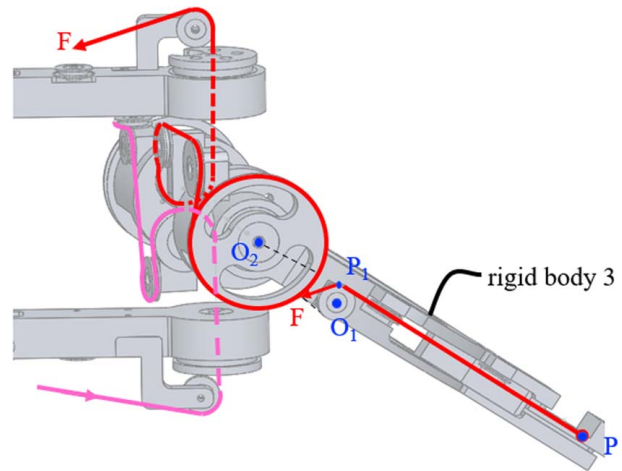


**Fig. 6 Drive cable routes for X-axis rotation of rigid body 3 (Color version online.)**

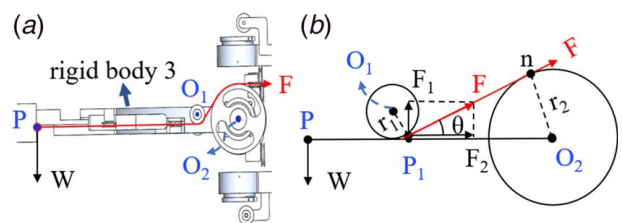


**Fig. 7 Relationship between the tensile force on the driving cable and the payload (Color version online.)**



the cable is common tangent to the circles (pulleys) centered at  $O_1$  and  $O_2$ , respectively. The tension  $F$  of the cable is divided into  $F_1$  and  $F_2$ , and  $F_1$  provides the moment of rotation of rigid body 3:

$$F_1 = F \cdot \sin \theta = F \cdot \frac{r_2}{\overline{P_1 O_2}} \quad (1)$$

Moment balance can be achieved as follows:

$$W \cdot \overline{P O_2} - F_1 \cdot \overline{P_1 O_2} = 0 \rightarrow \therefore F = \frac{\overline{P O_2}}{r_2} \cdot W \quad (2)$$

where the length of  $\overline{P O_2}$  is 0.2 m, and the radius  $r_2$  is 0.0155 m. By substituting the above formula with these numeric data, we get  $F = 12.9W$ . In other words, the tension of drive cable is required 12.9 times force greater than the lifted weight. Therefore, the payload of the proposed tensegrity shoulder joint is calculated as  $W = F/12.9$  when the tension  $F$  is given, under the assumption of no frictional loss. Let us assume the payload to be  $W = 1 \text{ kg}_f = 9.8 \text{ N}$  for the calculation of the tensile strength of the cable. According to Eq. (2), the tension  $F$  of the drive cable is calculated as  $F = 12.9W = 126.42 \text{ N}$ . Using the material specifications reported in Ref. [20], the tensile strength of the drive cable when 1 kg<sub>f</sub> payload is applied is calculated as follows:

$$\sigma = \frac{F}{\text{area}} = \frac{126.42}{\pi \times 0.0004064^2} = 2.4365 \times 10^8 \text{ N/m}^2$$

where the tensile strength of the drive cable is approximately 28.3% of the breaking tensile strength ( $8.5864 \times 10^8 \text{ N/m}^2$ ) of the material.

**3.4 Kinematics.** The output angle of the motor is denoted by  $\theta_i$  and the diameter of the output shaft by  $D_i$ . The corresponding joint angle is  $q_i$  and the diameter of the joint axis is  $J_i$ . Now, the following relationship between motor angle and joint angle can be obtained as  $q_i = (D_i/J_i)\theta_i$ . For the proposed tensegrity shoulder system, the output shaft diameters of each motor are designed as  $D_1 = 21 \text{ mm}$ ,  $D_2 = 14 \text{ mm}$ , and  $D_3 = 14 \text{ mm}$ . The corresponding diameters of the joint axis are  $J_1 = 21 \text{ mm}$ ,  $J_2 = 19 \text{ mm}$ , and  $J_3 = 31 \text{ mm}$ . Now, we have the relationships between the motor angles and the joint angles such as  $q_1 = \theta_1$ ,  $q_2 = 0.737\theta_2$ , and  $q_3 = 0.452\theta_3$ .

Let us assign the reference coordinate frames as shown in Fig. 8, with each axis passing through a rotation axis, for which  $M_1$  drives the Z-axis rotation,  $M_2$  drives the Y-axis rotation, and  $M_3$  drives the X-axis rotation. According to the established coordinate frames, the Z–Y–X Euler angles method is adopted to solve the forward kinematics [21]. Also, the endpoint of  $P = [p_x, p_y, p_z]^T$  is calculated by multiplying the rotation matrix and the zero position  $P_0 = [0, L, 0]^T$ . Now, the rotation matrix and position vector can be combined for the special Euclidean group  $SE(3)$  and it is also called

the homogeneous transformation matrix  $T \in SE(3)$ :

$$T = \begin{bmatrix} r_{11} & r_{12} & r_{13} & p_x \\ r_{21} & r_{22} & r_{23} & p_y \\ r_{31} & r_{32} & r_{33} & p_z \\ 0 & 0 & 0 & 1 \end{bmatrix} = \begin{bmatrix} c_1 c_2 & c_1 s_2 s_3 - s_1 c_3 & c_1 s_2 s_3 + s_1 s_3 & L(c_1 s_2 s_3 - s_1 c_3) \\ s_1 c_2 & s_1 s_2 s_3 + c_1 c_3 & s_1 s_2 s_3 - c_1 s_3 & L(s_1 s_2 s_3 + c_1 c_3) \\ -s_2 & c_2 s_3 & c_2 c_3 & L c_2 s_3 \\ 0 & 0 & 0 & 1 \end{bmatrix} \quad (3)$$

where  $r_{ij}$  implies  $i$ th row and  $j$ th column element of  $3 \times 3$  rotation matrix  $R$ ,  $c_i = \cos(q_i)$ , and  $s_i = \sin(q_i)$  for  $i = 1, 2, 3$ . From the above formula, it can be seen that the workspace of point  $P$  is a surface of the sphere with a radius  $L$ . In this case, an inverse kinematics solution is easily obtained from the Z–Y–X Euler angles method as follows:

$$q_1 = \tan^{-1} \frac{r_{21}}{r_{11}}, \quad q_2 = \tan^{-1} \frac{-r_{31}}{\sqrt{r_{11}^2 + r_{21}^2}}, \quad q_3 = \tan^{-1} \frac{r_{32}}{r_{33}} \quad (4)$$

## 4 Experiments

To validate the performance of the proposed tensegrity shoulder system, the motion tracking experiments were conducted in the task space. The control scheme runs on a STEP2 PC (manufactured by Neuromecka Co.) with an Intel Core Celeron Braswell 1.6 GHz CPU and 4GB RAM. The Elmo Solo Whistles were used as the motor drivers and connected to STEP2 via EtherCAT communication. A proportional-derivative (PD) position controller is applied to three degrees-of-freedom tensegrity shoulder mechanism.

$$\tau = K_P[(q_d - q) + T_D(\dot{q}_d - \dot{q})] \quad (5)$$

where  $\tau$  is the input torque,  $K_P$  is the proportional gain, and  $T_D$  is the derivative time. The Ziegler–Nichols first method [22] using the slope and time delay of step-response was adopted for control gain tuning. The acquired PD gain parameters per joint are listed in Table 1.

**4.1 Curved Trajectory Generation in Task Space.** Since the endpoint  $P$  of the proposed shoulder system is able to move along the surface of a sphere with radius  $L$ , it is necessary to use a curved trajectory along the sphere surface rather than a straight line due to the workspace limitation. The target pose is composed of six variables, which contain three Cartesian coordinates and three Euler angles, and expressed as homogeneous transformation  $SE(3)$  as suggested in the previous section. Since the proposed tensegrity shoulder system has only three degrees-of-freedom, however, there exist three constraints in some position and orientation. Thus, the components of  $SE(3)$  can be divided into three dependent variables  $p_z$ ,  $R_x$ , and  $R_y$  and three independent variables  $p_x$ ,  $p_y$ , and  $R_z$ , where  $p_i$  and  $R_i$  stand for the  $i$ -axis element of position vector  $P$  and the  $i$ th column vector of the rotation matrix  $R$ , respectively, for  $i = x, y, z$ . Once the desired trajectories of the independent variables are generated, the dependent trajectories can be calculated by the constraints. The desired trajectories for independent variables

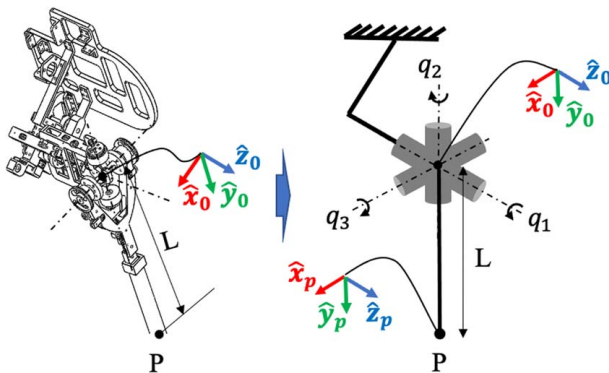


Fig. 8 Kinematics of the proposed tensegrity shoulder system

Table 1 Gain tuning results using Ziegler–Nichols first method

Joint $i$	Delay $d$	Slope $s$	$K_P = \frac{1.2}{d \cdot s}$	$T_D = 0.5d$
1	0.005	1.965	122.137	0.0025
2	0.013	1.656	55.755	0.0065
3	0.009	1.438	92.720	0.0045

are defined as follows:

$$p_{x,d}(s) = p_{x,start} + s(t)(p_{x,end} - p_{x,start}) \quad (6)$$

$$p_{y,d}(s) = p_{y,start} + s(t)(p_{y,end} - p_{y,start}) \quad (7)$$

$$R'_{z,d}(s) = R_{z,start} + s(t)(R_{z,end} - R_{z,start}) \quad (8)$$

where the subscript  $d$  implies the desired trajectories of each independent variable, start and end stand for the starting and ending positions of the desired trajectories, respectively, and  $s(t) \in [0, 1]$  denotes the time scaling parameter having a fifth-order polynomial of time:

$$s(t) = 10\left(\frac{t}{t_f}\right)^3 - 15\left(\frac{t}{t_f}\right)^4 + 6\left(\frac{t}{t_f}\right)^5 \quad (9)$$

for  $0 \leq t \leq t_f$ . Once the desired positions  $p_{x,d}$  and  $p_{y,d}$  are generated from Eqs. (6) and (7), the desired  $p_{z,d}$  is calculated from the spherical constraint of  $p_{z,d} = \sqrt{L^2 - p_{x,d}^2 - p_{y,d}^2}$ . In addition, the desired Z-axis rotation  $R'_{z,d}$  is already generated from Eq. (8), but it is not guaranteed to be a unit vector, so it needs to be normalized as follows:

$$R_{z,d} = \frac{R'_{z,d}}{\|R'_{z,d}\|} \in \mathfrak{R}^3 \quad (10)$$

As shown in Fig. 8, the unit vector from the coordinate origin to the end point  $P$  indicates the direction of Y-axis rotation, thus we have

$$R_{y,d} = \frac{P_d}{\|P_d\|} \in \mathfrak{R}^3 \quad (11)$$

where  $P_d = [p_{x,d}, p_{y,d}, p_{z,d}]^T$ . Since  $R_{y,d}$  and  $R_{z,d}$  are orthonormal from each other,  $R_{x,d}$  can then be obtained from the cross product of two vectors:

$$R_{x,d} = R_{y,d} \times R_{z,d} \quad (12)$$

By collecting all the variables, we can construct the desired homogeneous transformation  $T_d$  as follows:

$$T_d = \begin{bmatrix} R_{x,d} & R_{y,d} & R_{z,d} & P_d \\ 0 & 0 & 0 & 1 \end{bmatrix} \in SE(3) \quad (13)$$

After getting the desired homogeneous transformation  $T_d$  from the desired trajectories and constraints, the inverse kinematic solutions of Eq. (4) are used to convert the desired task coordinates  $T_d$  to the desired joint coordinates  $q_d$ . Also, we need the desired joint velocity  $\dot{q}_d$  for the controller implementation. For this purpose, the desired twist  $V_d$  at endpoint  $P$  is calculated using the matrix logarithm [21]:

$$[V_d] = \log(T^{-1}T_d) \quad (14)$$

where  $[V_d]$  is  $SE(3)$  form of the six-dimensional desired twist  $V_d \in \mathfrak{R}^6$ . For example, if  $V_d = [\omega_d^T, v_d^T]^T$ , then  $[V_d] = \begin{bmatrix} [\omega_d] & v_d \\ 0_{1 \times 3} & 0 \end{bmatrix}$ , where  $[\omega_d]$  implies the skew-symmetric matrix of  $\omega_d \in \mathfrak{R}^3$ . Furthermore, we can get the desired joint velocity using the pseudoinverse matrix of Jacobian

$$\dot{q}_d = J^\dagger V_d \quad (15)$$

where  $J^\dagger$  denotes the pseudoinverse of Jacobian. Now,  $q_d$  and  $\dot{q}_d$  are applied to the controller of Eq. (5) to follow the desired trajectories of the endpoint of the proposed tensegrity system.

**4.2 Experimental Results.** The simulation was conducted using the MATLAB to validate the effectiveness of the curved trajectory generation. The target poses of the endpoint were selected as

**Table 2 Sequential four target poses for trajectory generation, where  $\alpha$ ,  $\beta$ , and  $\gamma$  represent Euler angles about X axis, Y axis, and Z axis, respectively**

$i$	$p_x$ (m)	$p_y$ (m)	$p_z$ (m)	$\alpha$ (rad)	$\beta$ (rad)	$\gamma$ (rad)
1	0.0386	0.2187	0.222	-0.1745	0	0.7854
2	0.2187	0.0386	0.222	-0.1745	-0.7854	1.5708
3	-0.0386	0.2187	0.222	-0.1745	0	2.3562
4	0.2187	-0.0386	0.222	-0.1745	0.7854	1.5708

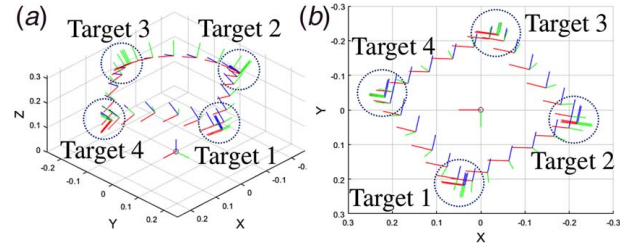


**Fig. 9 Desired trajectory generation: (a) in the 3D space and (b) in the frontal (XY-plane) view**

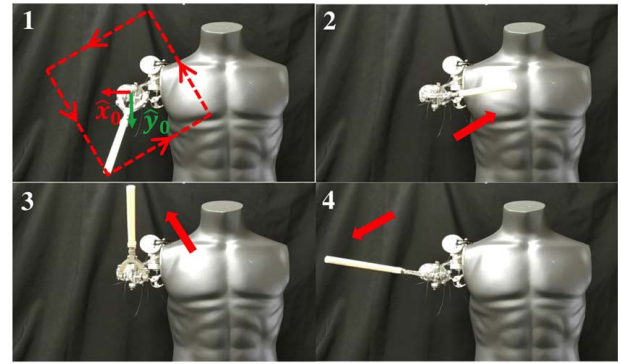


**Fig. 10 Consecutive movements of the proposed tensegrity shoulder system along four target poses in the task space**

four points to draw a square shape in the XY-plane view. The sequential four target poses of the endpoint  $P$  are listed in Table 2. The simulation result for trajectory generation is presented in Fig. 9, in which Fig. 9(a) shows that the desired trajectory is well generated along the sphere surface in three-dimensional space and Fig. 9(b) shows the position in the XY-plane in the frontal view.

Next, the experiment regarding the proposed tensegrity shoulder system was conducted. The experimental results by applying the desired trajectory and the PD control are shown in Figs. 10 and 11. The endpoint of the proposed tensegrity shoulder system well followed the quadrilateral trajectory. Especially, Fig. 11 represents the position of endpoint  $P$  and each of the joint angle tracking results. The actual joint angles are measured by the encoder in motor module, and the actual position is calculated using the forward kinematics. For the control, the desired joint angles are obtained using the inverse kinematics from the desired trajectory. In Fig. 11, the vertical blue line stands for the start of each motion segment, and the time duration of each motion segment is 1 s. The tracking errors are shown in Figs. 11(b) and 11(d); in which the average joint errors were  $\tilde{q}_1 = 0.0137$ ,  $\tilde{q}_2 = 0.0487$ , and  $\tilde{q}_3 = 0.0313$  rad, and the average position error were  $\tilde{p}_x = 0.0131$ ,  $\tilde{p}_y = 0.0086$ , and  $\tilde{p}_z = 0.0056$  m. Finally, the experimental results were posted as a video clip<sup>2</sup>. In addition, the authors would like

<sup>2</sup><http://www.youtube.com/watch?v=y07iGXqbHsk>

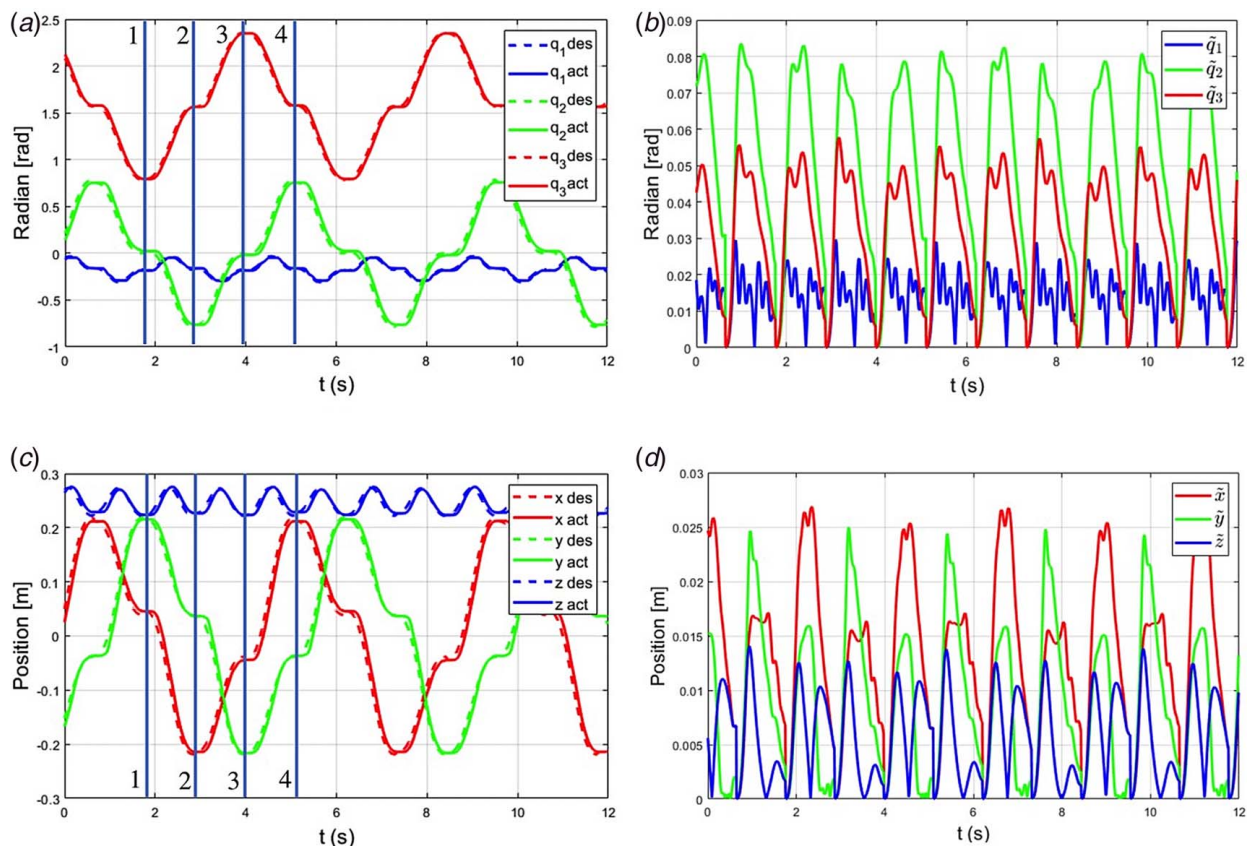


**Fig. 11 Experimental results for trajectory tracking performance, where (a) joint angle tracking performance, (b) joint tracking error as absolute value, (c) endpoint tracking performance, and (d) endpoint tracking error as absolute value, in which “des” and “act” in the graph legend stand for the desired values and the actual values, respectively (Color version online.)**

to mention the stiffness of the proposed mechanism on the tracking performance. In the gravitational direction, the stiffness of the mechanism was measured as 2450 N/m, and it influences the motion accuracy due to the relatively low stiffness when the load is applied to the endpoint. For example, the tracking error will be increased by 2 mm when 0.5 kg<sub>f</sub> load is applied to the endpoint in the gravitational direction.

## 5 Conclusions

In this paper, we have addressed a three degrees-of-freedom tensegrity shoulder mechanism and its control system. For this purpose, three rigid bodies were connected by using 16 strings, so that rigid bodies did not make contact with each other, and thus the proposed tensegrity shoulder mechanism belonged to the class 1 tensegrity system. The proposed tensegrity shoulder mechanism could mimic the ranges of human shoulder joint motions. Moreover, the proposed mechanism could be made using fewer materials, and thus, the shoulder mechanism could be manufactured in a light-weight fashion, which could reduce the inertial effects as well. And the proposed tensegrity structure with a mechanism was driven by the cable-driven motors.

**5.1 Discussions and Future Works.** In developing the tensegrity shoulder joint mechanism, we found several issues to be dealt with in the subsequent studies. First, it was very hard to fix the cables while maintaining high tension. For this purpose, any device to maintain the tension constantly should be developed when the cables were fixed. Second, the cable was often fractured when lifting higher loads or handling higher joint torques. There

exists a trade-off between the thickness of the cable and easy manufacturing. For example, if the cable thickness increases to improve the higher force capability, the cable routing would be much difficult because the curvature of the cable decreases according to the thickness increase. Third, how to calculate the cable length variations should be devised to understand how the stiffness of the mechanism is affected. Finally, an external measurement experiment using a motion capture system is required to quantify the effects of the tensegrity suspension on the accuracy of joint axes as well as to analyze the subsequent transfer of joint axis misalignment into position error.

## Acknowledgment

This work was supported in part by the National Research Foundation of Korea under Grant No. 2019R1A2C1088375, and in part by the Technology Innovation Program funded by the Korean Government (MTIE) under Grant No. 20008908, and in part by the National Natural Science Foundation of China under Grant No. 62073108.

## Conflict of Interest

There are no conflicts of interest.

## Data Availability Statement

No data, models, or code were generated or used for this paper.



## References

- [1] Guo, J., Xiang, C., Helps, T., Taghavi, M., and Rossiter, J., 2018, "Electroactive Textile Actuators for Wearable and Soft Robots," IEEE International Conference on Soft Robotics (RoboSoft), Livorno, Italy, Apr. 25–27, pp. 339–343.
- [2] Kim, J. H., Li, Z. Y., Choi, H. R., Moon, H., and Koo, J. C., 2016, "Design of Flexible Joint Using in Soft Robot Hand," 13th International Conference on Ubiquitous Robots and Ambient Intelligence (URAI), Xian, China, Aug. 19–22, pp. 101–103.
- [3] Somm, L., Hahn, D., Kumar, N., and Coros, S., 2019, "Expanding Foam as the Material for Fabrication, Prototyping and Experimental Assessment of Low-Cost Soft Robots With Embedded Sensing," *IEEE Robot. Autom. Lett.*, **4**(2), pp. 761–768.
- [4] Florez, J. M., Shih, B., Bai, Y., and Paik, J. K., 2014, "Soft Pneumatic Actuators for Legged Locomotion," IEEE International Conference on Robotics and Biomimetics (ROBIO 2014), Bali, Indonesia, Dec. 5–10, pp. 27–34.
- [5] O'Neill, C. T., Phipps, N. S., Cappello, L., Paganoni, S., and Walsh, C. J., 2017, "A Soft Wearable Robot for the Shoulder: Design, Characterization, and Preliminary Testing," International Conference on Rehabilitation Robotics (ICORR), London, UK, July 17–20, pp. 1672–1678.
- [6] Qi, R., Lam, T. L., and Xu, Y., 2014, "Mechanical Design and Implementation of a Soft Inflatable Robot Arm for Safe Human–Robot Interaction," IEEE International Conference on Robotics and Automation (ICRA), Hong Kong, China, June 1–5, pp. 3490–3495.
- [7] Jantsch, M., Wittmeier, S., Dalamagkidis, K., Panos, A., Volkart, F., and Knoll, A., 2013, "Anthrob—A Printed Anthropomorphic Robot," 13th IEEE-RAS International Conference on Humanoid Robots (Humanoids), Atlanta, GA, Oct. 15–17, pp. 342–347.
- [8] Nakanishi, Y., Asano, Y., Kozuki, T., Mizoguchi, H., Motegi, Y., Osada, M., Shirai, T., Urata, J., Okada, K., and Inaba, M., 2012, "Design Concept of Detail Musculoskeletal Humanoid Kenshiro," 12th IEEE-RAS International Conference on Humanoid Robots (Humanoids), Osaka, Japan, Nov. 29–30, pp. 1–6.
- [9] Lessard, S., Bruce, J., Jung, E., Teodorescu, M., Sunspirai, V., and Agogino, A., 2016, "A Lightweight, Multi-Axis Compliant Tensegrity Joint," IEEE International Conference on Robotics and Automation (ICRA), Stockholm, Sweden, May 16–21, pp. 630–635.
- [10] Lessard, S., Castro, D., Asper, W., Chopra, S. D., Teodorescu, M., Sunspirai, V., and Agogino, A., 2016, "A Bio-Inspired Tensegrity Manipulator With Multi-DOF, Structurally Compliant Joints," IEEE/RSJ International Conference on Intelligent Robots and Systems (IROS), Daejeon, South Korea, Oct. 9–14, pp. 5515–5520.
- [11] Rasheed, T., Long, P., and Caro, S., 2020, "Wrench-Feasible Workspace of Mobile Cable-Driven Parallel Robots," *ASME J. Mech. Rob.*, **12**(3), p. 031009.
- [12] Lessanibahri, S., Cardou, P., and Caro, S., 2020, "A Cable-Driven Parallel Robot With an Embedded Tilt-Roll Wrist," *ASME J. Mech. Rob.*, **12**(2), p. 021107.
- [13] Mustafa, S. K., and Agrawal, S. K., 2012, "Force-Closure of Spring-Loaded Cable-Driven Open Chains: Minimum Number of Cables Required & Influence of Spring Placements," IEEE International Conference on Robotics and Automation (ICRA), Saint Paul, MN, May 14–19, pp. 1482–1487.
- [14] Mao, Y., and Agrawal, S. K., 2012, "Design of a Cable-Driven Arm Exoskeleton (CAREX) for Neural Rehabilitation," *IEEE Trans. Robot.*, **28**(4), pp. 922–931.
- [15] Yang, Y., Chen, W., Wu, X., and Chen, Q., 2010, "Stiffness Analysis of 3-DOF Spherical Joint Based on Cable-Driven Humanoid Arm," 5th IEEE Conference on Industrial Electronics and Applications, Taichung, Taiwan, June 15–17, pp. 99–103.
- [16] Lum, G. Z., Mustafa, S. K., Lim, H. R., Lim, W. B., Yang, G., and Yeo, S. H., 2010, "Design and Motion Control of a Cable-Driven Dexterous Robotic Arm," IEEE Conference on Sustainable Utilization and Development in Engineering and Technology, pp. 106–111.
- [17] Lugo, J. H., Ramadoss, V., Zoppi, M., Cannata, G., and Molino, R., 2019, "Modeling of a Cable-Based Revolute Joint Using Biphasic Media Variable Stiffness Actuation," 3rd IEEE International Conference on Robotic Computing (IRC), Naples, Italy, Feb. 25–27, pp. 618–623.
- [18] Skelton, R. E., and de Oliveira, M. C., 2009, *Tensegrity Systems*, Springer, New York.
- [19] Levangie, P. K., and Norkin, C. C., 2011, *Joint Structure and Function: A Comprehensive Analysis*, 5th ed., F. A. Davis/Jaypee Brothers, New Delhi.
- [20] Stainless Steel Cable, Bare 7x49, Commercial, <http://www.savacable.com/stainless-steel-cable-bare-7x49-commercial/>, Accessed July 31, 2021.
- [21] Lynch, K. M., and Park, F. C., 2017, *Modern Robotics*, Cambridge University Press, Cambridge, MA.
- [22] Franklin, G. F., Powell, J. D., and Emami-Naeini, A., 2002, *Feedback Control of Dynamic Systems*, Prentice Hall, Upper Saddle River, NJ.